ORIGINAL PAPER

A simplified method to estimate the distribution of lateral forces acting on stabilizing piles in c–φ soil slopes

Ning Bao[1] · Jian-feng Chen[1] · Rui Sun[1]

Abstract

The downslope movement of sliding soils usually leads to a nonlinear distribution of lateral forces on stabilizing piles in a row. Precise prediction of the lateral forces is of significance to assess the stability of pile-reinforced soil slopes. A simplified pressure-based method is presented for estimating the lateral force distribution on piles embedded in a semi-infinite c–φ inclined soil slope. The soil arching theory was incorporated to calculate the driving forces transferred onto piles after determining the active lateral earth pressure between adjacent piles through the horizontal slice method. Several published experimental and numerical studies were selected to examine the applicability of the proposed method. It is demonstrated that the predicted result is in good agreement with the observed data in terms of both the shape and the magnitude of the distribution of lateral forces. The parametric study further indicates that the distribution of lateral forces along the depth changes from nonlinear to planar as slope angle increases, whereas the other parameters, such as friction angle, soil cohesion, pile spacing and depth of unstable soil layer, mainly influence its magnitude. The proposed method could be employed in the preliminary prediction of response of piles with scarce design parameters.

Keywords Stabilizing pile · c–φ soil slope · Lateral force distribution · Horizontal slice method · Soil arching effect

List of symbols

c	Soil cohesion (kPa)
C	A constant to be calculated with boundary conditions (kPa/m)
d	Pile diameter (m)
D_1	Center-to-center pile spacing (m)
D_2	Clear pile spacing ($D_2 = D_1 - d$) (m)

✉ Jian-feng Chen
   jf_chen@tongji.edu.cn

   Ning Bao
   ningbao2020@tongji.edu.cn

   Rui Sun
   sr-tjut@tongji.edu.cn

[1]   Department of Geotechnical Engineering, College of Civil Engineering, Tongji University, Shanghai 200092, China

h	Height of the application of resultant lateral force (m)
H	Depth of the unstable soil layer (m)
H_{cal}	Calculated soil depth corresponding to the critical slope angle (m)
H_i	Depth of the ith soil sublayer (m)
K_p	Rankine passive earth pressure coefficient (dimensionless)
l_i	Length of the segmental slip plane of the ith sublayer (m)
l_{mi}	Average length of top and bottom planes of the ith sublayer (m)
L_i	Length of the top plane of the ith sublayer (m)
L_{i-1}	Length of the bottom plane of the ith sublayer (m)
n	Number of sublayers (dimensionless)
p_a	Lateral force per unit depth carried by the pile (kN/m)
p_i	Active earth pressure acting on the ith sublayer (kPa)
p_i'	Horizontal component of p_i (kPa)
P_t	Resultant lateral force carried by the pile (kN/pile)
q_i	Vertical earth pressure distributed on the top plane of the ith sublayer (kPa)
q_{i-1}	Vertical pressure distributed on the bottom plane of the ith sublayer (kPa)
q_{sur}	Surcharge (kPa)
r	Radial distance of the selected crown element (m)
R_i	Reaction force from stable soils acting on the ith sublayer (kN)
R_{in}	Inner radius of the arching zone (m)
R_{out}	Outer radius of the arching zone (m)
S_i	Area of the ith sublayer (m^2)
T_0, T_1	Calculation parameters (m^2)
U_0, U_1, U_3	Calculation parameters (dimensionless)
w_i	Self-weight of ith sublayer ($w_i = \gamma S_i$) (kN/m)
α	Integral argument (°)
β	Slope angle (°)
β_{crit}	Critical slope angle to be calculated with boundary conditions (°)
γ	Soil unit weight (kN/m^3)
θ_i	Inclination angle of segmental slip plane of the ith sublayer (°)
σ_{hi}'	Horizontal component of σ_{vi} (kPa)
σ_{in}	Radial stress distributed on the inner arch boundary (kPa)
σ_{out}	Radial stress distributed on the outer arch boundary (kPa)
σ_r	Radial stress distributed on the selected crown element (kPa)
σ_{vi}	Effective stress on soil element (kPa)
σ_{vi}'	Vertical component of σ_{vi} (kPa)
σ_θ	Tangential stress distributed on the selected crown element (kPa)
φ	Friction angle of soil (°)
HSM	Horizontal slice method

1 Introduction

For the past decades, the pile stabilization method has come into widespread use to rein-
force the slopes which are identified to be potentially unstable (Poulos 1995; Ellis et al.
2010; Wang 2013; Smethurst et al. 2020). The piles work passively to resist the driving
forces of sliding soils and transfer them downward to the underlying stable stratum sub-
jected to the action of flowing soils. Bearing on sufficient lateral forces, the piles may

produce significant internal forces even to failure (Al-Defae and Knappett 2014). In this context, an appropriate estimation of the distribution of lateral forces acting on the piles arising from the sliding mass is therefore necessary for improving the design of piles and slope stabilization.

Some analytical methods are available in the literature for evaluating the mechanical response of a row of piles to laterally moving soils, and they are generally classified into two different types, namely the displacement-based method and the pressure-based method (Jeong et al. 2003; Kourkoulis et al. 2012). The former method treats the interactive soil–pile system as beams on elastic foundations (Ashour and Ardalan 2012). The soil–pile interaction is represented by the p–y curve after solving the fourth-order differential equation in which pile deflections and lateral soil displacements are inevitably needed. Nevertheless, it is worthwhile noting that it is quite difficult to detect soil deformation accurately from in situ measurements, apart from referring to the numerical results and empirical correlations in similar cases (Jeong et al. 2003). The pressure-based method provides an alternative option for assessing the behavior of the laterally loaded piles especially for a lack of sufficient soil displacement data, although it is intended for the ultimate limit state (Muraro et al. 2014; Pirone and Urciuoli 2018).

Among the existing pressure-based methods, the plastic deformation approach presented by Ito and Matsui (1975) is generally employed to estimate the lateral force applied to the piles in a row when considering the stability of pile-reinforced soil slopes (Hassiotis et al. 1997; Deng and Yang 2019). Notwithstanding the significant contribution of the plastic deformation theory, such an approach cannot accurately predict the shape of lateral force distribution acting on the pile segment above the failure surface in that it directly uses the Rankine active earth pressure coefficient to calculate the active lateral earth pressure but ignores the rotation of principal stresses due to the arching effect. Previous research has revealed that the lateral force per unit depth develops nonlinearly during the progressive lateral force loading rather than the triangular or trapezoidal distribution illustrated by Ito and Matsui's method (Cai and Ugai 2000; Liu et al. 2020; Wang et al. 2021). The resulting discrepancy of lateral forces turns out to be more significant at a larger depth, and meanwhile influences the accurate prediction of the resultant forces and its height of application. Similar problems can also be found in the improved plastic deformation method (Kumar and Hall, 2006) and the rigid-plastic method (RPM) (Pirone and Urciuoli, 2018).

Limited closed-form analytical solutions have been presented regarding the nonlinear distribution of lateral forces resting on the piles. He et al. (2015a) integrated the plastic deformation method with the vertical arching theory for effectively estimating the distribution of lateral forces on a pile in sandy slopes, except a limited accuracy in terms of generally overestimating the experimental and numerical test results. Zhu et al. (2016) rederived the soil stress relationship in the vertical arching zone by modifying the lateral earth pressure coefficient in the formulation presented by He et al. (2015a), but the modified solution is still highly conservative. In addition, most natural deposits are characterized by some degree of cohesion on account of fine contents (Iskander et al. 2013). However, these two methods aforementioned do not pertain to c–φ soil slopes where c is soil cohesion and φ is friction angle, because the influence of soil cohesion on the slip plane which defines the sliding wedge is not considered in the vertical arching theory. Up to now, the response of piles in c–φ soil slopes still cannot be predicted accurately through the existing pressure-based methods.

For considering the arching effect in the determination of stress redistribution, this paper proposed a novel pressure-based method to predict the distribution of lateral forces on stabilizing piles which were embedded into c–φ soil slopes. First, the sliding wedge

enclosed by the curved slip plane was determined. Then, based on the horizontal slice method (HSM), the active lateral earth pressure between adjacent piles induced by the sliding wedge was presented. Finally, the active lateral earth pressure was substituted into the horizontal arch model to obtain the lateral forces along each pile. Several published model tests, numerical simulations and case histories were selected to examine the applicability of the proposed methodology. A parametric study was further carried out concerning the slope angle (β), soil strength parameters (c and φ), pile spacing (D_2/D_1) and the depth of unstable soil layer (H).

2 Theoretical analysis

In the proposed analytical model, some basic simplifications and assumptions are made as follows: (a) The slope soil is homogeneous and isotropic; (b) the piles are rigid inclusions in a semi-infinite slope; (c) the unstable soil mass deforms in a plane strain condition along the depth; (d) the stress state in the semi-circular arch is uniform. In addition, to simplify the calculation of the lateral earth pressure between adjacent piles, another assumption proposed by He et al. (2015a) is also adopted that the sliding wedge is defined within the shadow portion shown in Fig. 1a, and the shape of sliding wedge is discussed later. Considering the symmetric nature of the problem, the stress state in a limited zone between the centerlines of adjacent piles is analyzed, mirroring Ito and Matsui (1975). The piles have the same diameter of d and are arranged in a row with a center-to-center spacing of D_1.

2.1 Profile of sliding wedge

Determination of the profile of the sliding wedge is crucial for accurately analyzing the stress state of soil elements and predicting the active lateral earth pressure between adjacent piles. Paik and Salgado (2003) assumed the sliding wedge behind a retaining wall had a slip plane with an inclination angle of $45° + \varphi/2$ to the horizontal, and named it the vertical arching zone. Zhu et al. (2016a) further examined the slip plane in pile-reinforced inclined sandy slopes after analyzing the stress relation of soil elements through the pole point theory. However, the effect of soil cohesion on the shape of slip plane was not considered in these assumptions.

HSM has the capacity of accommodating complex working conditions. Lin et al. (2008) employed this method successfully to predict the stress field adjacent to the rigid wall. Ashour and Ardalan (2012) also incorporated this method into the developed strain wedge model to calculate the lateral soil pressure on the piles. The HSM is herein formulated to compute the active lateral earth pressure per unit depth caused by the sliding wedge. The sliding wedge is equally divided into n scalene trapezoids along the depth. The top and bottom sides of each trapezoid are parallel to the sloping surface with an inclination angle β, as depicted in the cross section UU′ shown in Fig. 1b. The increment of each sublayer is measured as $\Delta H = H/n$.

A soil element I within the ith sublayer, at a depth H_i below the sloping surface, is represented in an enlarged view. The stress state on this element consists of the modified effective stress σ_{vi} on planes ab and $a'b'$ oriented at an inclination angle β to the vertical, and σ_{hi} on planes aa' and bb' oriented at a same angle β to the horizontal. The vertical component of σ_{vi} can be obtained through Eq. (1).
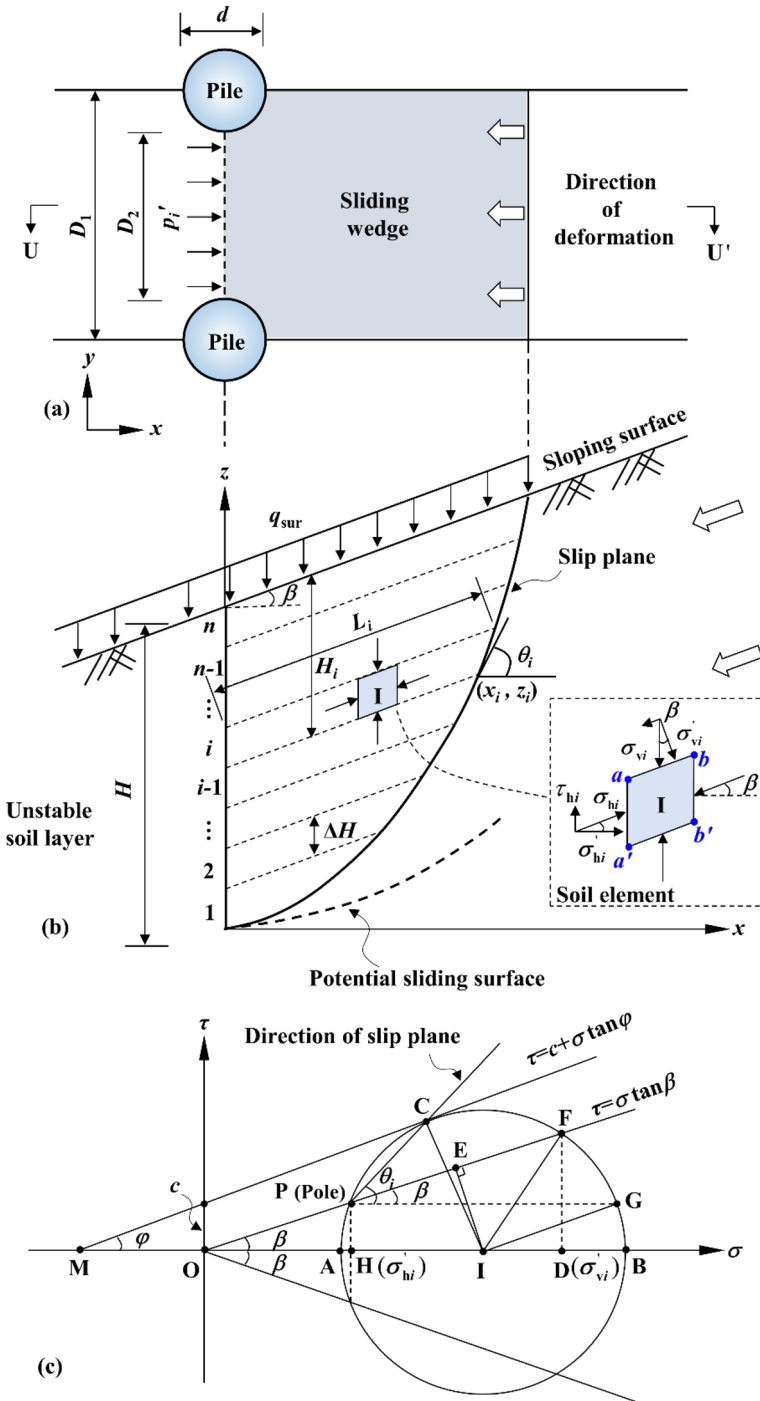
Fig. 1 An analytical model of the soil–pile interaction: **a** plan view of the sliding mass between adjacent piles. (adapted from He et al. 2015a); **b** profile of cross section UU′ with multiple sublayers; **c** the Mohr's circle representation of the stress state on soil element I

$$\sigma'_{vi} = \sigma_{vi} \cos \beta = \gamma H_i \cos^2 \beta \tag{1}$$

where $\gamma =$ the unit weight of soils; $H_i = (n - i + 1)\Delta H$ for $1 \le i \le n$.

Figure 1c shows the Mohr circle representation of the stress state on element I which is used to derive the geometric relationship of relevant stresses. In the principal stress space, the failure envelope is drawn as the line MC for given soil strength parameters (i.e., c and φ) satisfying the Mohr–Coulomb failure criterion. Stresses of σ_{hi} and σ_{vi} are then determined through the projected line starting from the origin at an inclination angle β to the horizontal and intersecting the Mohr's circle at points P and F. The direction of the slip plane at the ith sublayer can then be represented as the line PC based on the theory of pole point, and the inclination angle θ_i is determined as:

$$\theta_i = \angle CPF + \beta = (\angle CIE + \angle EIF)/2 + \beta \tag{2}$$

where $\angle CIE = \varphi - \beta$; $\angle EIF = \arccos (l_{IE}/l_{IF})$. According to the geometric relationship of the triangle ΔOIE and ΔMIC, $l_{IE} = l_{OI} \sin \beta$, $l_{IF} = l_{IC} = (l_{OI} + c \cot \varphi) \sin \varphi$. Equation (2) is then rewritten as:

$$\theta_i = \frac{1}{2}\left[\varphi + \beta + \arccos \left(\frac{l_{OI} \sin \beta}{c \cos \varphi + l_{OI} \sin \varphi}\right)\right] \tag{3}$$

To get l_{OI}, it is found $l_{IF}^2 = l_{ID}^2 + l_{DF}^2$ in the triangle ΔFID. And $l_{ID} = \sigma'_{vi} - l_{OI}$, $l_{DF} = \sigma'_{vi} \tan \beta$. Substituting them into Eq. (3) and simplifying, it then follows that:

$$l_{OI} = \left(A_i - \sqrt{B_i + C_i}\right)/\cos^2 \varphi \tag{4}$$

where $\begin{cases} A_i = \gamma H_i \cos^2 \beta + c \sin \varphi \cos \varphi \\ B_i = \gamma^2 H_i^2 \cos^2 \beta \left(\cos^2 \beta - \cos^2 \varphi\right) \\ C_i = c^2 \cos^2 \varphi + c \gamma H_i \cos^2 \beta \sin (2\varphi) \end{cases}$.

It is found from Eqs. (3) and (4) that for sandy soils, i.e., $c = 0$, the inclination angle of slip plane responding to ith sublayer can be written as $\theta_i = [\varphi + \beta + \arccos (\sin \varphi / \sin \beta)]/2$, which is consistent with the result obtained from He et al. (2015a). Whereas for c–φ soils, θ_i is also influenced by soil cohesion and the unit weight and changes with depth. The profile of the sliding wedge enclosed by the curved slip plane can be determined (Eq. 5) after calculating a series of coordinate pairs of endpoints of each sublayer in the xoz plane.

$$\begin{cases} x_i = L_i \cos \beta \\ z_i = i\Delta H + L_i \sin \beta \end{cases} \tag{5}$$

where $L_i = \Delta H \sum_{j=1}^{i} \frac{\cos \theta_j}{\sin (\theta_j - \beta)}$, which denotes the length of the top boundary of ith sublayer.

It is also found from Eq. (4) that $B_i + C_i < 0$ as β is larger than a critical value β_{crit}. The HSM is not effective until $\beta < \beta_{crit}$. Based on the mathematical requirement of $B_i + C_i \ge 0$, β_{crit} is determined as:

$$\cos^4 \beta + \left(-\cos^2 \varphi + \frac{2c}{\gamma H} \sin \varphi \cos \varphi\right) \cos^2 \beta + \left(\frac{c}{\gamma H}\right)^2 \cos^2 \varphi \ge 0 \tag{6}$$

Solving Eq. (6) for β_{crit}, and noting that it should be the minimum one (Eq. 7).

$$\beta_{\text{crit}} = \arccos \sqrt{\frac{\cos^2 \varphi}{2} - \frac{c}{\gamma H} \cdot \frac{\sin 2\varphi}{2} - \varphi \left[\left(\frac{c}{\gamma H} \cdot \frac{\sin \varphi}{2} - \frac{\cos \varphi}{2} \right)^2 - \left(\frac{c}{\gamma H} \right)^2 \right]^{1/2}}$$

(7)

The calculated soil depth H_{cal} must also be changed to accommodate the reduction of the volume of the sliding wedge for $\beta > \beta_{\text{crit}}$. At this moment, H_{cal} is derived from $B_i + C_i = 0$ and shown in Eq. (8):

$$H_{\text{cal}} = \frac{c}{\gamma} \cdot \frac{\cos \varphi \sin (\varphi + \beta)}{\cos \beta (\cos^2 \varphi - \cos^2 \beta)}$$

(8)

2.2 Calculation of lateral earth pressure

The concept of the HSM is to treat each sublayer as a rigid body satisfying the force and moment equilibrium requirements. Figure 2 displays all force components acting on the ith sublayer with four corners labeled as e, f, g and h. The succeeding formulations follow the horizontal and vertical force equilibrium requirements and the moment balance requirement to the midpoint of the plane gh with an inclination angle of θ_i, and can be expressed as:

$$p_i \Delta H \cos \varphi + c l_i \cos \theta_i - R_i \cos \left(\pi/2 - \varphi + \theta_i \right) = 0$$

(9)

$$w_i + q_i L_i - c \Delta H - R_i \sin \left(\pi/2 - \varphi + \theta_i \right) - c l_i \sin \theta_i - q_{i-1} L_{i-1} - p_i \Delta H \sin \varphi = 0$$
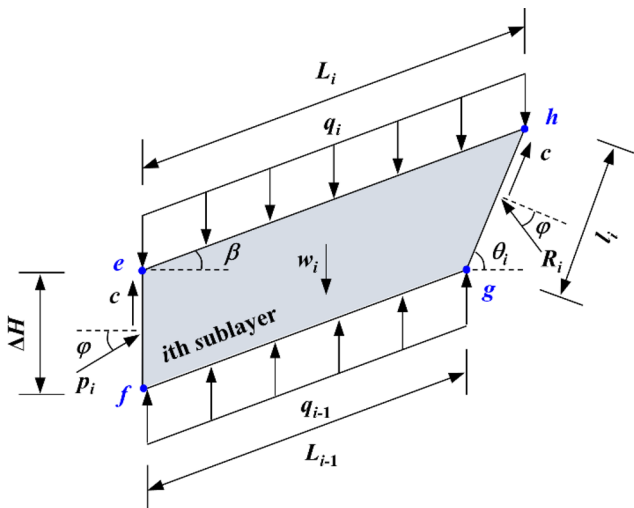
(10)

Fig. 2 Force components acting on the ith sublayer

$$q_{i-1}L_{i-1}\left(L_{i-1}\cos\beta + l_i\cos\theta_i\right)/2 + c\Delta H\cos\beta l_{mi} + p_i\Delta H l_{mi}\sin\left(\varphi - \beta\right)$$
$$-\gamma S_i l_{mi}\cos\beta/2 - q_i L_i\left(L_i\cos\beta - l_i\cos\theta_i\right)/2 = 0 \tag{11}$$

where

p_i = The active earth pressure of ith sublayer;

R_i = The reaction force from soils outside of the sliding wedge;

q_i, q_{i-1} = The vertical pressure acting on the planes eh and fg, respectively;

$l_i = \Delta H\cos\beta/\sin\left(\theta_i - \beta\right)$, which denotes the length of the line gh;

$l_{mi} = \left(L_i + L_{i-1}\right)/2$, which denotes the average length of the top and bottom boundaries;

$S_i = l_{mi}\Delta H\cos\beta$, which denotes the area of ith sublayer;

$w_i = \gamma S_i$, which denotes the self-weight of ith sublayer.

Solving Eqs. (9) and (10) for p_i, it follows that:

$$p_i = \frac{\sin\left(\theta_i - \varphi\right)}{\Delta H\cos\left(2\varphi - \theta_i\right)} \times \left[q_i L_i - q_{i-1}L_{i-1} + \gamma S_i - c\Delta H - \frac{cl_i\cos\varphi}{\sin\left(\theta_i - \varphi\right)}\right] \tag{12}$$

The sliding wedge-induced lateral earth pressure is considered to be the horizontal component of p_i and can then be calculated as Eq. (13).

$$p_i' = \frac{\sin\left(\theta_i - \varphi\right)\cos\varphi}{\Delta H\cos\left(2\varphi - \theta_i\right)} \times \left[q_i L_i - q_{i-1}L_{i-1} + \gamma S_i - c\Delta H - \frac{cl_i\cos\varphi}{\sin\left(\theta_i - \varphi\right)}\right] \tag{13}$$

Its distribution along the depth can then be represented in an iterative computation scheme to satisfy the boundary loading condition, i.e., $q_0=0$ at $i=1$ and $q_n = q_{sur}$ at the sloping surface.

Substituting Eq. (12) into Eq. (11), the recursive relationship between q_{i-1} and q_i is obtained through Eq. (14).

$$q_{i-1} = q_i U_0 + \gamma\Delta H U_1 + c U_2 \tag{14}$$

where the calculation parameters U_0, U_1, U_2 are dimensionless and expressed as:

$U_0 = T_0/T_1$,

$U_1 = \frac{l_{mi}^2\cos\beta}{T_1}\left[2\sin\left(\varphi - \beta\right)\sin\left(\theta_i - \varphi\right) - \cos\beta\cos\left(2\varphi - \theta_i\right)\right]$,

$U_2 = \frac{2l_{mi}}{T_1}\left\{\Delta H\left[\cos\beta\cos\left(2\varphi - \theta_i\right) - \sin\left(\varphi - \beta\right)\sin\left(\theta_i - \varphi\right)\right] - l_i\cos\varphi\sin\left(\varphi - \beta\right)\right\}$;

T_0 and T_1 are expressed in m^2,

$T_0 = 2l_{mi}L_i\sin\left(\varphi - \beta\right)\sin\left(\theta_i - \varphi\right) - L_i\cos\left(2\varphi - \theta_i\right)\left(L_i\cos\beta - l_i\cos\theta_i\right)$,

$T_1 = 2l_{mi}L_{i-1}\sin\left(\varphi - \beta\right)\sin\left(\theta_i - \varphi\right) - L_{i-1}\cos\left(2\varphi - \theta_i\right)\left(L_{i-1}\cos\beta + l_i\cos\theta_i\right)$.

2.3 Soil arching effect behind piles

2.3.1 Description of the horizontal arch model

The horizontal arching effect is another reinforcing mechanism of pile-reinforced slopes. It usually accompanies the "flow mode" failure originally proposed by Viggiani (1981), where the unstable soils become plastic and flow around piles. A larger proportion of
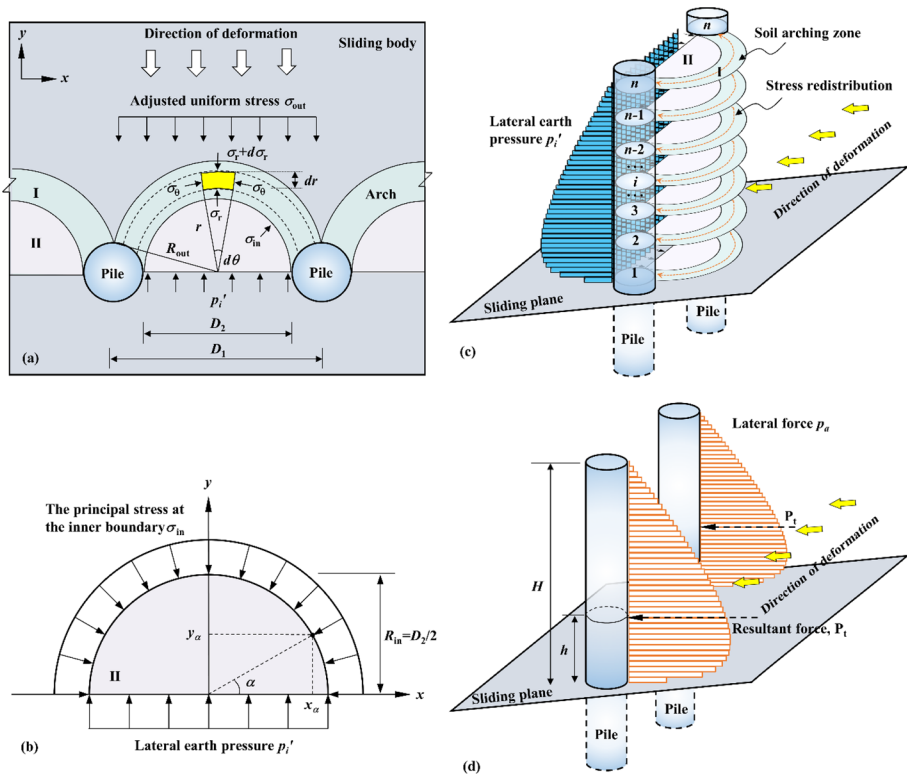
Fig. 3 Analytical model of the horizontal soil arch: **a** schematic representation of the soil arch; **b** uniform stress distribution in zone II; **c** lateral earth pressure distribution between adjacent piles; **d** lateral force distribution acting on the piles

driving forces at this zone is transferred to the piles along the arch path while less on soil masses between adjacent piles. This load transferring behavior guaranteed the stability of the slope (Liang and Zeng 2002; Kourkoulis et al. 2012). To quantify the arching behavior in pile-reinforced slopes, much current research has been directed at the model tests (Kahyaoglu et al. 2012) and numerical simulations (Li et al. 2013), whereas the theoretical analysis of the arch model in a three-dimensional condition is still rare. Li et al. (2020) developed a composite analytical model for estimating the earth pressure against laggings, which consisted of the upper arch zone and the lower soil wedge. However, an obvious pressure discontinuity was observed at the interface linking the two soil failure zones. Zhao et al. (2020) developed the wedge theory by assuming the arch shape to be an isosceles right triangle with arch height being constant along the depth, while the distribution of lateral forces on a pile cannot be evaluated.

In this section, the horizontal arch model is proposed to estimate the lateral forces arising from the unstable soil mass on each pile. A semi-circular arch shape is adopted to define the arching area, referring to the arching analysis of the piled embankment (Hewlett and Randolph 1988; Low et al. 1994; Van Eekelen et al. 2013), underground tunneling (Lin et al. 2019), and retaining walls (Paik and Salgado 2003). Figure 3a shows the schematic representation of horizontal soil arch model with a thickness half

of the pile diameter. In practice, the arch height may feature a decreasing trend along the depth due to the influence of multiple internal and external factors. Unfortunately, there is still not an unified approach to describe this trend up to now except referring to the numerical analysis. In addition, the variation of the arch height would be expected to complicate the arching analysis significantly. Zhao et al. (2020) indicated that the load on the retaining structure calculated by the constant arch height was acceptable because the change of arch height caused less difference within the limited soil depth. As a result, the arch height is assumed to be constant along the depth as shown in Fig. 3c.

2.3.2 Stress redistribution in the arching zone

In Fig. 3a, the inner radius of the arching zone is $R_{in} = D_2/2$ in which D_2 is the pile clear spacing, while the outer radius is computed as $R_{out} = \sqrt{(D_1/2)^2 + (d/2)^2}$. The volumes per unit depth at the crown element are represented individually: the top volume $dV_0 = (r + dr)d\theta dz$, the bottom volume $dV_1 = rd\theta dz$, and the side volume $dV_2 = drdz$. It is assumed that the stress state in the arch is uniform so that the limit state can occur in the entire arch (Van Eekelen et al. 2013; Rui et al. 2022). Thereafter, the equation of the radial equilibrium is expressed as:

$$\left(\sigma_r + d\sigma_r\right)dV_0 - \sigma_r dV_1 - 2\sigma_\theta dV_2 \sin\frac{d\theta}{2} = 0 \tag{15}$$

where σ_r is the radial stress; σ_θ is the tangential stress; r is the radial distance.

The influence of γ on the equilibrium of forces is not incorporated in Eq. (15), because the inertial force is perpendicular to the radial direction. By substituting the volume components of the crown element illustrated above into Eq. (15) and then simplifying through $\sin\frac{d\theta}{2} \approx \frac{d\theta}{2}$, it follows that:

$$\frac{d\sigma_\theta}{dr} + \frac{d\sigma_r}{r} + \frac{\sigma_r - \sigma_\theta}{r} = 0 \tag{16}$$

Neglecting the term with a product of more than one increment, Eq. (16) is simplified into:

$$\frac{d\sigma_r}{dr} + \frac{\sigma_r - \sigma_\theta}{r} = 0 \tag{17}$$

For limit analysis of c–φ soil, the tangent stress is determined as $\sigma_\theta = K_p\sigma_r + 2c\sqrt{K_p}$, where K_p is the Rankine passive earth pressure coefficient $K_p = (1 + \sin\varphi)/(1 - \sin\varphi)$. Replacing them into Eq. (17), it can then be rewritten as:

$$\frac{d\sigma_r}{dr} + \frac{\left(1 - K_p\right)\sigma_r}{r} = \frac{2c\sqrt{K_p}}{r} \tag{18}$$

The general solution of Eq. (18) is provided below.

$$\sigma_r = Cr^{(K_p-1)} + \frac{2c\sqrt{K_p}}{1 - K_p} \tag{19}$$

The boundary conditions at the inner and outer boundaries are then computed from Eq. (19).

$$\sigma_{\text{in}} = \sigma_{r=D_2/2} = C\left(\frac{D_2}{2}\right)^{(K_p-1)} + \frac{2c\sqrt{K_p}}{1-K_p} \tag{20a}$$

$$\sigma_{\text{out}} = \sigma_{r=R_{\text{out}}} = CR_{\text{out}}^{(K_p-1)} + \frac{2c\sqrt{K_p}}{1-K_p} \tag{20b}$$

where C is a constant, which can be determined through the force equilibrium condition in Zone II; σ_{in} is the radial stress distributed on the inner arch boundary; σ_{out} is the radial stress distributed on the outer arch boundary.

As shown in Fig. 3b, the equation of the vertical force equilibrium is expressed as:

$$\int \sigma_{\text{in}} \sin\alpha \, ds \, dz = p_i' D_2 dz \tag{21}$$

where $\alpha \in [0, \pi]$; $\begin{cases} x_\alpha = D_2\cos\alpha/2 \\ y_\alpha = D_2\sin\alpha/2 \end{cases}$; $ds = \sqrt{d^2x_\alpha + d^2y_\alpha} = \frac{D_2}{2}d\alpha$.

After integrating the principal stresses along the inner arch boundary which are mathematically represented by Eq. (20a), Eq. (21) is solved as $\sigma_{\text{in}} = p_i'$. The constant C relates the stresses in the arching zone (e.g., σ_{in} and σ_{out}) to lateral earth pressure p_i' and can be written as $C = \left(p_i' - \frac{2c\sqrt{K_p}}{1-K_p}\right) \times \left(\frac{2}{D_2}\right)^{(K_p-1)}$.

As a result, the lateral force per unit depth p_{ai} transferred onto the piles because of arching, can be calculated by subtracting the lateral force on the soil mass between adjacent piles (i.e., *yoz* plane at $x=0$) from the driving force on the outer arch boundary (Eq. 20b), on the basis of such an assumption that an uniform distribution of pressures is applied onto the outer arch boundary (Low et al. 1994).

$$p_{ai} = \sigma_{\text{out}}D_1 - p_i'D_2 \tag{22}$$

Then the resultant lateral force P_t acting on the piles can be obtained by the summation of the lateral force acting on each sublayer:

$$P_t = \Delta H \sum_{i=1}^{n} p_{ai} \tag{23}$$

In the case of the nonlinear characteristics of lateral forces along the depth illustrated in Fig. 3d, the height of application of the resultant lateral force h is defined as the moment of lateral force on each sublayer around the base of the unstable soil layer to the resultant lateral force, and is written as:

$$h = \frac{\Delta H \sum_{i=1}^{n} p_{ai}(H - H_i)}{P_t} \tag{24}$$

2.4 Calculation procedure of the distribution of lateral forces on piles

In summary, the calculation procedure of the proposed method is plotted in Fig. 4, which can be achieved via a MATLAB tool. It is shown in Fig. 4 that a limited number of input
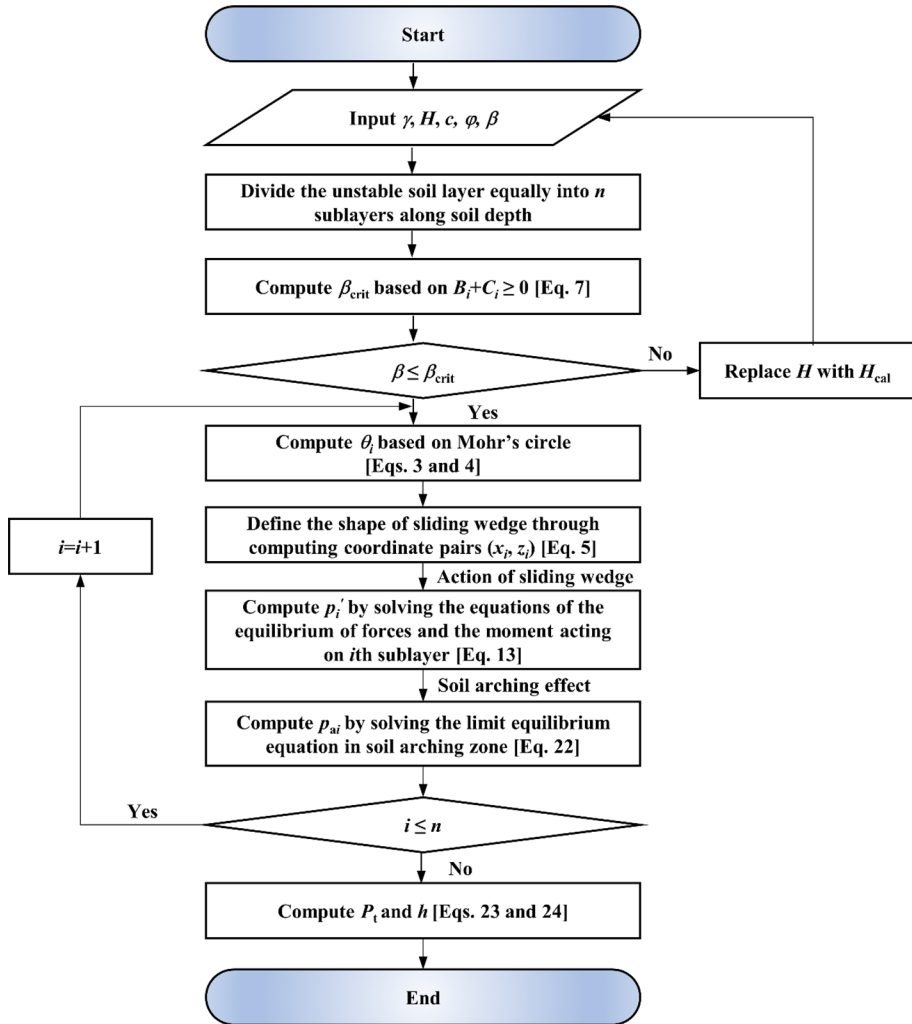
Fig. 4 Flowchart of the calculation procedure

parameters are required, indicating the proposed method can readily be employed in the preliminary prediction of the response of piles. Compared to the calculation procedure proposed by He et al. (2015a), the improved plastic deformation method by Kumar and Hall (2006) and the rigid-plastic method by Pirone and Urciuoli (2018), the present method has three main distinctions:

(1) The assumed slip plane enclosing the sliding wedge is mathematically proved to be nonlinear as a function of slope angle, soil strength parameters, and soil depth.
(2) The HSM is employed to calculate the active lateral earth pressure on the soil mass between adjacent piles. Compared to the vertical arching theory, the HSM can comprehensively consider the effect of slope angle and cohesive strength on the distribution of the lateral earth pressure after undergoing an implicit process.

(3) Regarding the conservative feedback from the plastic deformation method, the three-dimensional arch model is developed to redistribute the driving forces of sliding soils onto the piles.

3 Method verification

To validate the applicability of the proposed method, three experimental case histories involving the model test and field trials, and two numerical simulations were selected from the literature for comparison in this section. The results are presented in terms of the distribution of lateral forces acting on the pile segments above the failure plane.

3.1 Comparison with model test

Guo and Ghee (2006) designed a new apparatus to evaluate the response of piles undergoing lateral soil movements. Figure 5a shows the sectional view of the test apparatus. The model consisted of the shear box and loading system, in which the box had an internal dimension of 1 m by 1 m, and 0.8 m in height. A total of 16 laminar aluminum frames were piled up to constitute the upper moveable box with a thickness of 0.4 m. In the laboratory test, medium coarse quartz sand was gradually filled into the upper shear box through a sand pluviation technique to achieve a uniform density of 16.27 kN/m³. The corresponding soil friction angle was determined to be 35.5° at a relative density of 0.89 by means of the direct shear test. Two piles made of aluminum tubes were individually instrumented with ten pairs of strain gauges, which were arranged in a center-to-center spacing of $D_1 = 96$ mm ($D_1/d = 3$). After the piles were simultaneously driven into the lower fixed box to a specific depth of 300 mm, the rectangular loading block was driven by a hydraulic jack to push the
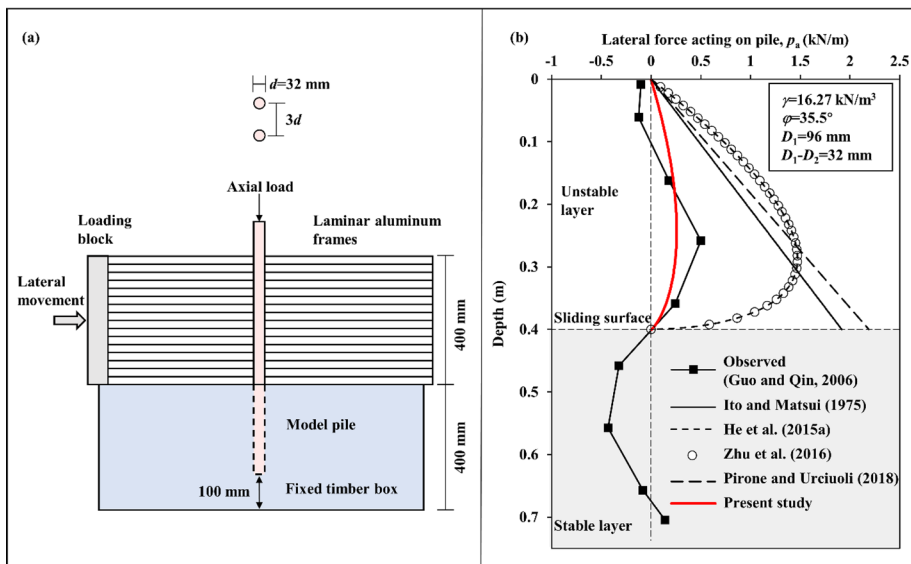
Fig. 5 Lateral force distribution on piles from the model test: **a** schematic representation of test apparatus. (adapted from Guo and Qin, 2006); **b** comparison of the experimental and calculated results

upper box forward at an increment of 10 mm until 60 mm. As the lateral displacement (w_s) increased from 30 to 40 mm, it was found that the piles horizontally translated about 7 mm, which indicated that the soil ultimate resistance has been reached. Consequently, the pile response at $w_s = 30$ mm was selected to validate the proposed method as shown in Fig. 5b.

The changes in lateral forces acting on the piles were characterized by a gradual increase to 0.24 kN/m within a depth of 0.24 m followed by a reduction to nil. This behavior agreed with the typical trend reported by Guo and Ghee (2006). As seen from the model test results, negative lateral forces developed near the pile top. It was considered to be the result of pile deformation and non-uniform soil movement. Conversely, the piles were assumed to be rigid in the present analytical model without any deflection under soils flowing around. Therefore, only positive lateral forces were obtained from Eq. (22). On the other hand, predictions of several other pressure-based methods were also plotted in Fig. 5b. The predictions of He et al. (2015a) and Zhu et al. (2016) overlapped each other under the horizontal ground surface, and gave a similar result as the present method in terms of the shape of the lateral force distribution. However, they significantly overestimated the maximum lateral force acting on the piles by 194% compared to the observed data. As for the other two approaches, i.e., methods by Ito and Matsui (1975) and Pirone and Urciuoli (2018), the predicted lateral forces increased linearly along the depth, and the value discrepancy with the experimental data grew obviously at a larger depth. Therefore, the proposed method had a higher accuracy compared to the earlier analytical methods.

3.2 Comparison with numerical method

Two numerical cases of sandy slopes stabilized with piles were employed to validate the proposed method. Using the finite difference program Flac3D, Lier (2012) developed a numerical model of a pile-reinforced slope based on the Masseria Marino mudslide in Italy. Figure 6a shows the simulated portion of the slope characterized by 300 m in length, 8 m in width and 11° in inclination. It consisted of the sliding body having a thickness of 4.5 m, the imposed shear zone of 0.5 m, and the stable layer of 20 m. Three piles with a diameter of 0.4 m were installed in a row in the middle of the slope. The interval between adjacent piles was $D_1 = 0.9$ m and $D_2 = 0.5$ m. The soils and piles were modeled as the linear elastic perfectly plastic materials with Mohr–Coulomb failure criterion. The sliding body and shear zone were both assumed to be sandy soils with an identical density of 1900 kN/m³, but different friction angles of 28° and 25°, respectively. The stable stratum which was given sufficient soil strength served as a non-yielding layer. To reproduce the landslide process, the strength reduction technique was locally applied to the shear zone in terms of a gradual reduction of its shear strength. In comparison with the field measurements, the numerical model effectively predicted the pile response and gave an insight into the soil–pile interaction mechanism, such as the arching behavior. Detailed description of the simulation procedure and material properties could refer to Lier (2012).

Another numerical case study came from He et al. (2015a). They also performed a numerical simulation based on Flac3D software with the similar slope section, constitutive model, and the soil layer classification as Lier (2012) as shown in Fig. 6b. The main differences were as follows: the slope angle increased to 18.4°, the pile spacing to 3 m with a same pile diameter (i.e., $d = 0.4$ m), and the soil friction angle to 32°. Although the prescribed pile spacing ($D_1/d = 7.5$) was quite larger than both that of Lier (2012) and the suggested upper limit by Durrani et al. (2006), the typical arching phenomenon was also observed from the stress contour around piles. Liang and Zeng (2002) also found a critical
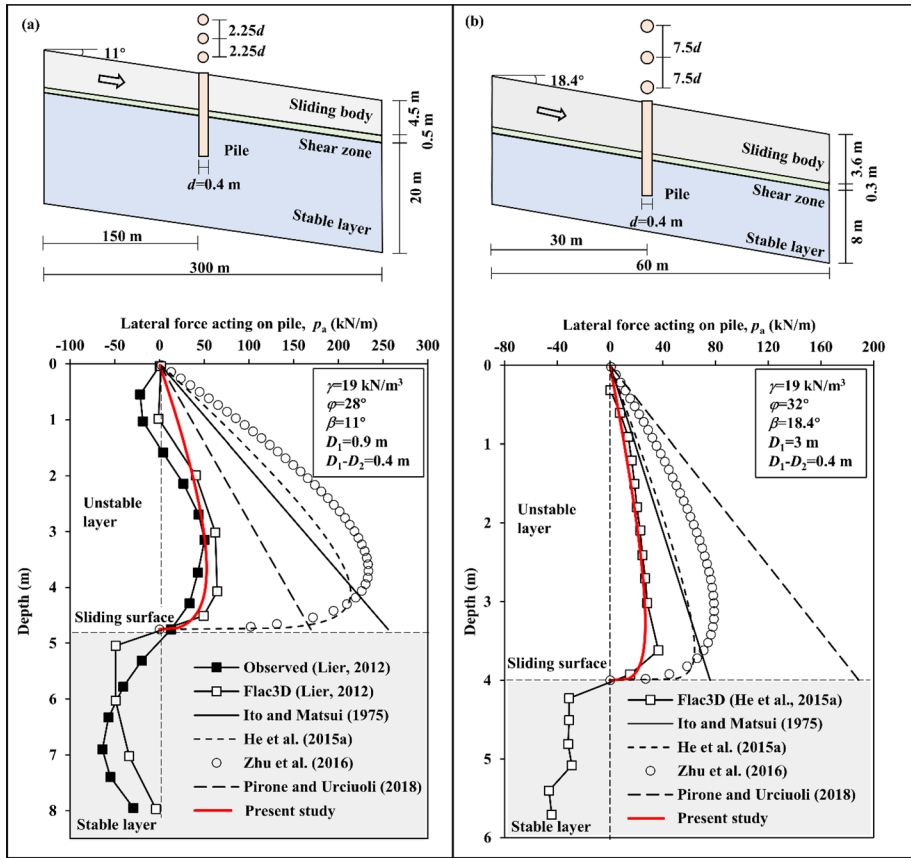
Fig. 6 Comparison of the numerical and calculated results: **a** with a slope angle of 11°; **b** with a slope angle of 18.4°

spacing as large as 8*d* for the arching effect taking place in sandy soils with a friction angle of 30°.

In Fig. 6, the calculated heights of the unstable soil layer in two numerical cases were set to 4.75 m and 4.0 m, respectively. In light of the thickness of shear zone much smaller than that of the unstable layer, its strength parameter (i.e., φ) was considered to be identical with the unstable layer. Both figures revealed that the predictions using the proposed method had a satisfactory agreement with the numerical results in terms of the shape and magnitude of distribution of lateral forces. In Fig. 6a, the difference in the predicted maximum lateral forces to the field data was as small as 2.1 kN/m. In Fig. 6b, the lateral force distribution curve matched well with most part of the numerical results.

It can also be seen that the other methods overestimated the lateral forces to different extents. For the case of sloping ground, Zhu et al. (2016) predicted larger lateral forces than He et al. (2015a) because the modified active earth pressure coefficient increased with slope angle, increased the lateral earth pressure and enhanced the squeezing effect between adjacent piles, which was contrary to the trend of that developed by He et al. (2015a). In Fig. 6a, the RPM approach developed by Pirone and Urciuoli (2018) gave smaller lateral

forces compared to the plastic deformation method, which was contrary to the result shown in Fig. 5. This can be explained that the ultimate lateral forces calculated from the RPM solution had a negative correlation with the slope angle for rigid-plastic soils, and consequently, the lateral forces in the sloping ground condition were primarily smaller than that in the horizontal ground condition. Additionally, at a larger pile spacing beyond the upper limit provided by Durrani et al. (2006), the RPM solution for pile rows was no longer applicable. Based on $\varphi = 32°$ in the study of He et al. (2015a), the critical pile spacing was calculated as $(D_1/d)_{crit} = 3.6$. Under such circumstance, Pirone and Urciuoli (2018) suggested that the equally spaced piles should be treated as isolated ones. The load transfer coefficient relating to the pile spacing in the RPM method was therefore modified to be K_p^2. The modified solution still overestimated the lateral forces acting on the piles as presented in Fig. 6b. It was worth noting that the proposed method also had a better adaptive behavior for a large pile spacing.

3.3 Comparison with field measurements

Two field trials on semi-infinite c–φ soil slopes were selected to validate the proposed method. The first was conducted on the Katamachi landslide area, one of the typical Tertiary landslides improved with stabilizing piles in Niigata, Japan (Ito and Matsui 1975). In the Katamachi landslide area, the clay layer of 6 m depth included rock fragments and slid slowly. The average unit weight was estimated to be 19 kN/m³. The shear strength of the clay layer was provided as $c = 25$ kPa and $\varphi = 2°$ from a shear test. Hollow reinforced concrete piles (diameter 300 mm, wall thickness 60 mm) were installed to prevent the continuous movement of the unstable soil layer. The piles in a row were placed at a center-to-center spacing of 4 m and inserted at a depth of 2.17 m into the shale layer. The upper clay layer of 2.17 m above the pile heads could be simplified as a uniform surcharge of 41.23 kPa. Electric gauges were installed in the piles, and the lateral force was then obtained by analyzing the measured strains in the piles.

The comparison of the observed and predicted lateral forces at the Katamachi landslide area is plotted in Fig. 7a. The calculated results from Ito and Matsui (1975) and He et al. (2015b) are also plotted in the same figure, in which the method proposed by He et al. (2015b) was typically used in the horizontal ground condition. Compared to the other two methods, the proposed method produced results that were in better agreement with the observed data.

Li et al. (2019) also presented a case history of Shabei-I slope stabilized with reinforced concrete piles. The study site was located in the north of Hongfeng Station on the Chengdu–Kunming Railway in Sichuan Province, China. The slope was measured 50 m width, 100 m length, and slope angle between 15 and 20°. The top soil layer of about 5 m thickness was identified to be unstable. The sliding soil consisted of the sand-clay mixed with gravel with soil cohesion of 19.6 kPa, friction angle of 10.6°, and an average unit weight of 19.1 kN/m³. Square concrete piles in a row were embedded through the sliding layer into the argillaceous siltstone. The piles had cross sections of 2 m by 2 m and were arranged at a center-to-center spacing of 4–5 m. Earth pressure cells were installed on the pile surface at an interval of 1 m, and the lateral thrust acting on the piles in the uphill direction was recorded after analyzing the measured horizontal earth pressure.
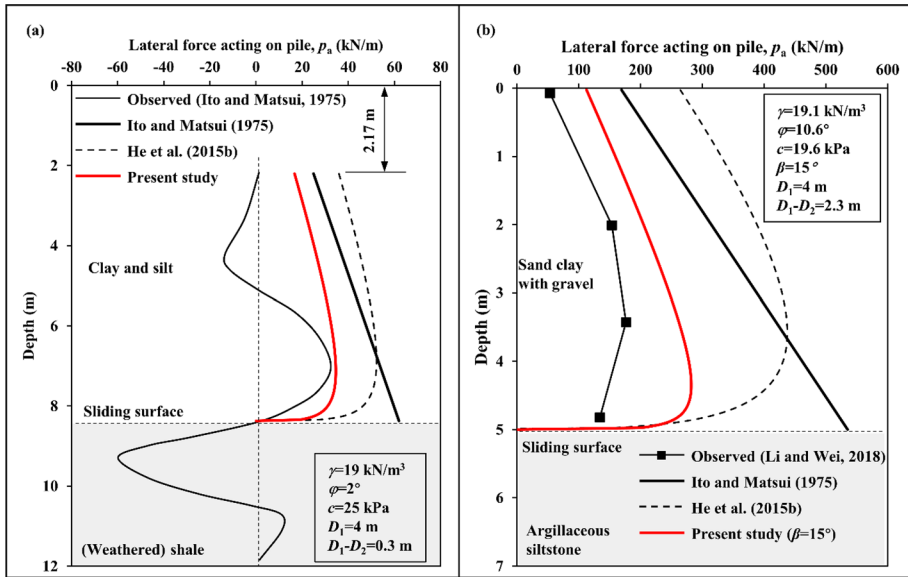
Fig. 7 Comparison of the field measurements and calculated results: **a** at Katamachi landslide area; **b** at Shabei-I slope

Square piles were generally considered to resist more lateral thrust. However, Liang and Zeng (2002) numerically found the additional lateral force applied to the square piles scarcely accounted for 5% of the resultant lateral force as long as the pile diameter of circular shafts was equal to the side length of square shafts. Wei et al. (2019) also found from the laboratory test of the landslide that at the same center-to-center spacing and the cross sectional area of the piles, square piles and circular piles behaved alike in terms of the bending moment distribution. Therefore, it can be drawn that the difference in mechanical behaviors of circular and square piles is limited and controllable. Based on these assumptions, the square pile problem can be equivalently transformed into a circular pile in a simple way.

Figure 7b compares the calculated lateral forces and the measurement results at Shabei-I slope. The pile diameter was calculated to be 2.3 m after an equivalent transformation as suggested by Wei et al. (2019). The slope angle was set to $\beta = 15°$. It can be found that the prediction using the proposed method increased first and then decreased to nil at the failure plane, which followed the trend of measurement results. The presence of soil cohesion as an additional contribution increased the lateral forces near the pile top compared to the results in sandy slopes as shown in Figs. 5 and 6. The method of He et al. (2015b) also presented the similar trend of the distribution of lateral force as the proposed method, however, it overestimated the field measurements in terms of the maximum lateral force by approximately 60% at the Katamachi landslide area and 148% at the Shabei-I slope. Ito and Matsui's method yield a smaller lateral force near the pile top, while the value discrepancy with the observed data was increasingly larger as the depth of the soil increased.

4 Parametric study

In this section, an extensive parametric study was conducted to analyze the effect of the variation of parameters on the lateral force distribution acting on the piles. The parameters considered included slope angle, soil friction angle, cohesion, pile spacing ratio (D_2/D_1) and the depth of unstable soil layer. Similar to the geometry of the slope and design parameters used in the numerical test of Lier (2012), the baseline values in the subsequent analysis were as follows: slope angle $\beta = 10°$, depth of unstable soil layer $H = 5$ m, friction angle $\varphi = 25°$, soil cohesion $c = 10$ kPa, soil density $\gamma = 19$ kN/m³, center-to-center spacing $D_1 = 1$ m, clear pile spacing $D_2 = 0.6$ m, and pile diameter $d = 0.4$ m. In what follows, these parameters were used throughout unless otherwise specified. By comparison, the results from the Ito and Matsui (1975) and He et al. (2015b) under the same input parameters were also evaluated in the same figure because the role of soil cohesion was represented in their formulations.

4.1 Effect of slope angle

Since the proposed method was based on the semi-infinite soil slope, the slope angle was therefore considered as one of the governing factors. Figure 8 shows the lateral force distribution along the depth with varying the slope angle and the corresponding slip planes along the typical cross section UU′. As can be seen, the distribution of lateral forces changed from triangular to nonlinear as the slope angle increased for $\beta \leq \beta_{crit}$, where $\beta_{crit} = 31.4°$ determined from Eq. (7). By comparison, the lateral force distribution in sandy soil slopes is also plotted in Fig. 8a. For sandy soil slopes, a larger slope angle caused a higher lateral force to the piles, especially for the portion below the depth of approximately $0.42H$, which agreed with the result observed by Zhu et al. (2016). However, due to the presence of soil cohesion, the increasing trend of p_a was also found near the pile top. On the other hand, the
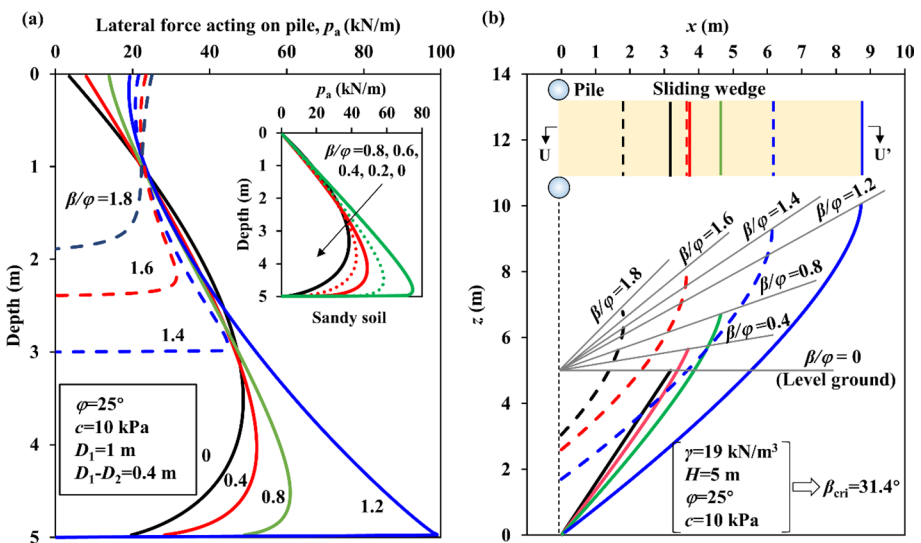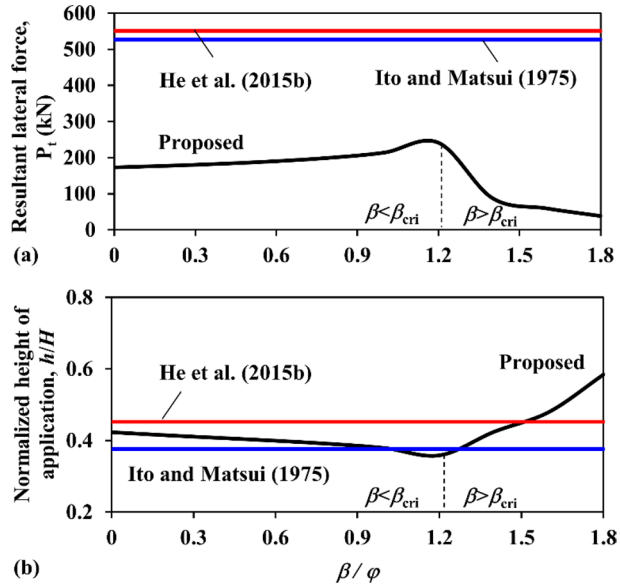

Fig. 8 Effect of slope angle: **a** on lateral force distribution along the depth; **b** on shape of slip plane along the cross section UU′

Fig. 9 Effect of slope angle: **a** on resultant lateral force; **b** on normalized height of application

slip plane enclosing the sliding wedge propagated away from the pile as the slope angle increased. Particularly, the slip plane behaved as a planar with an inclination angle of 57.5° for $\beta = 0$, consistent with the angle of the active slip plane which agreed with the assumption proposed by He et al. (2015b). For $\beta > \beta_{crit}$, the area of sliding wedge decreased due to the elevation of slip plane. As a result, the lateral earth pressure decreased, and the lateral forces transferred on the piles decreased as well.

The magnitude of the resultant lateral force acting on the piles and the height of the point of application, normalized with respect to the thickness of unstable soil layer, are plotted against the slope angle in Fig. 9. As shown in Fig. 9a, the resultant lateral force P_t calculated from Eq. (23) increased steadily to the maximum value greater than 240 kN/m as β arrived at β_{crit}, and then decreased quickly because of the reduction of sliding wedge. Also, the magnitude of P_t of the other two methods remained constant and had the same order of magnitude greater than 520 kN/m. This was attributed to the fact that the slope angle was not represented in their formulations. It is seen from Fig. 9b that the slope angle also had a slight influence on the centroid height of application calculated from Eq. (23). A slow decrease in the normalized height of application is observed in a narrow range of 0.38 and 0.45. This also implied that the corresponding pile segments may require some kind of additional enhancement for avoiding the bending failure.

4.2 Effect of friction angle

It is within the sliding body that the soil arching takes place. The arching behavior is dependent crucially on soil properties such as friction angle and cohesion (Cai and Ugai 2000; Chen and Martin 2002). Figure 10a shows the distribution of lateral forces acting on the piles with respect to friction angle in a range of $\varphi = 15$–40°. The shape of the distribution of lateral forces was nonlinear on which friction angle had less influence. But the depth to the maximum lateral force increased at a higher frictional strength. As a result, the
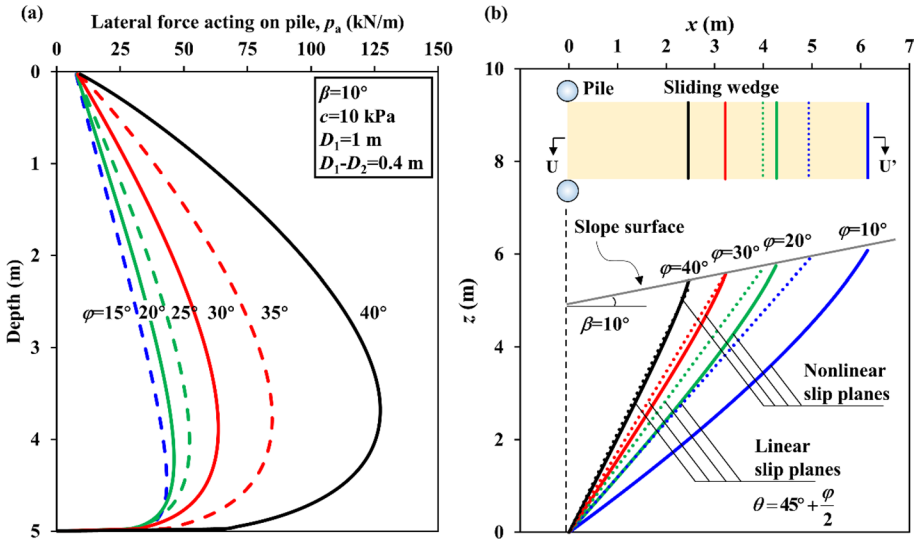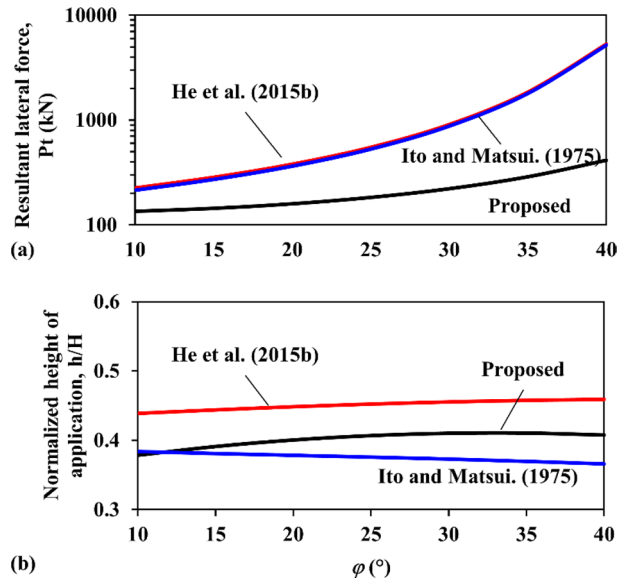
Fig. 10 Effect of soil friction angle: **a** on lateral force distribution along the depth; **b** shape of slip plane along the cross section UU′

Fig. 11 Effect of soil friction angle: **a** on resultant lateral force; **b** on normalized height of application

centroid of the lateral force distribution from the base of the sliding layer increased with increasing friction angle shown in Fig. 11b. Also, an increase in friction angle provided extra soil resistance, resulting in the additional frictional forces in the sliding soil masses. The rate of increase in lateral forces was faster as the friction angle increased. For example, the increment of the $p_{a, max}$ was 3.0 kN/m when φ increased from 15 to 20°, while $p_{a, max}$ rose to 42.5 kN/m when φ increased from 35 to 40°. In Fig. 10b, the increasing friction

angle resulted in an evolution of the shape of slip planes from nonlinear to planar, which ranged between the active slip plane with $\theta = 45° + \varphi/2$ ($= 50°$, $55°$, $60°$, $65°$ for $\varphi = 10°$, $20°$, $30°$, $40°$, respectively) and the linear one with $\theta = \left[\varphi + \beta + \arccos\ (\sin\varphi/\sin\beta)\right]/2$ ($= 10°$, $44.7°$, $54.8°$, $62.2°$ for $\varphi = 10°$, $20°$, $30°$, $40°$, respectively). Despite the decreasing trend of the sliding wedge during $15° \leq \varphi \leq 40°$, the lateral forces still increased. This was because the improvement of friction angle facilitated the granular interlocking and gave rise to a greater arching effect, transferring more load onto the piles (Liang and Zeng 2002).

Figure 11a shows the effect of friction angle on the resultant lateral force acting on the piles. There were more lateral forces resting on the piles for a higher friction angle. P_t from the methods of Ito and Matsui and He et al. increased quickly having negligible differences. The rate of increase in P_t estimated by the proposed method was far slower than the other two methods, especially for $30° \leq \varphi \leq 40°$. In Fig. 11b, the normalized heights of application from both He et al. (2015b) and the proposed method increased. While the value from Ito and Matsui decreased incrementally as small as 4.5% when the slope angle increased from 10 to 40°. It was because its distribution of p_a' was represented in the shape of the right-angle trapezoid calculated using the Rankine passive earth pressure coefficient, whose centroid geometrically showed a negative correlation with the ratio of the magnitude of lateral forces that was on the pile top to that on the bottom one near the failure plane.

4.3 Effect of cohesion

The distribution of lateral force under different cohesions is plotted in Fig. 12a. The soil cohesion had less influence on the shape of the distribution of lateral forces, but did have an influence on the magnitude of lateral forces. More driving forces were transferred
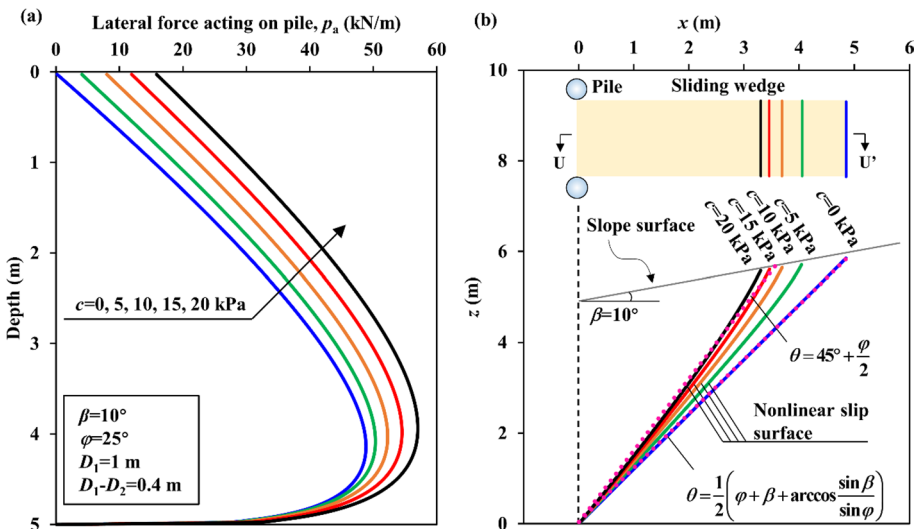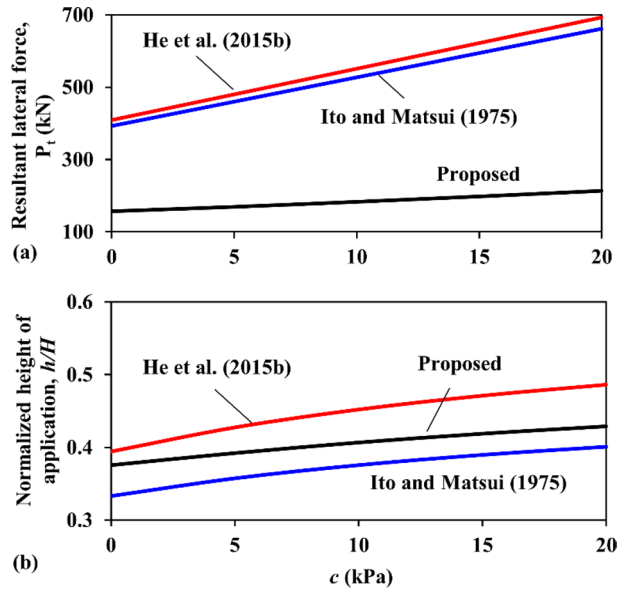

Fig. 12 Effect of cohesion: **a** on lateral force distribution along the depth; **b** shape of slip plane along the cross section UU′

Fig. 13 Effect of cohesion: **a** on resultant lateral force; **b** on normalized height of application

onto the piles as the cohesive strength increased. The c–φ soil slope induced lager lateral forces onto the piles than the sandy slope. Liang and Zeng (2002) also indicated that a relatively smaller cohesion value was required to develop a full arching at a narrower spacing. In addition, an increase in the cohesive strength also increased the initial inclination angle of slip planes along the cross section UU' as illustrated in Fig. 12b. The slip plane changed from planar to nonlinear and propagated closely toward the piles as soil cohesion increased. Notably, the inclination angle of the planar slip plane was $\theta = \left[\varphi + \beta + \arccos\left(\sin\varphi / \sin\beta\right)\right]/2(=50.4°)$ for $c = 0$ kPa. The leftward movement of slip plane, on the one hand, led to a decrease in the area of sliding wedge and, on the other hand, reduced the lateral earth pressure between adjacent piles.

In Fig. 13a, the resultant lateral force increased by 36.5% as c increased from 0 to 20 kPa, which was smaller than 68.6% from the method of Ito and Matsui and 69.2% from He et al. (2015a). The difference in P_t also indicated that the other two methods may overestimate the contribution of the soil cohesion to the lateral forces onto the piles. Also, as presented in Fig. 13b, the increment of lateral forces per unit depth induced by the soil cohesion decreased at a further depth, and consequently, the resulting centroid of the lateral force distribution rose from 0.37 to 0.43H.

4.4 Effect of pile spacing

Figure 14 shows the effect of pile spacing on the lateral force response of piles. The shape of the slip plane was assumed to be unchanged under different pile spacing in this study, and was already represented in Fig. 8b under the condition of $\varphi = 20°$ and $D_2/D_1 = 0.6$. As D_2/D_1 increased, the soil arching effect at a larger spacing was not as effective as in small spacing in terms of reducing the capacity of load transfer (Kahyaoglu et al. 2012; Liang et al. 2014). As a result, both the lateral force at any depth and the resultant lateral force decreased as the pile spacing tended to be narrower. Typically, the resultant lateral force applied on the piles for $D_2/D_1 = 0.8$ was 13% less than that for $D_2/D_1 = 0.2$. On the other
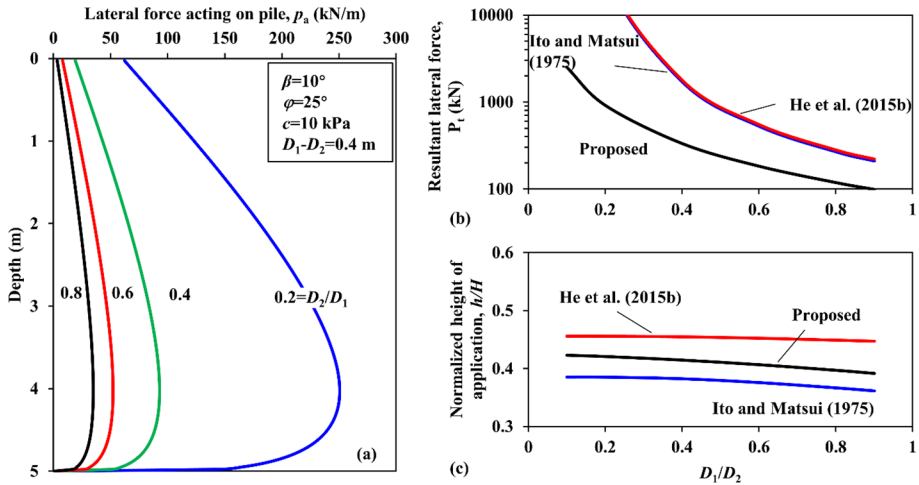
Fig.14 Effect of D_2/D_1: **a** on lateral force distribution along the depth; **b** on resultant lateral force; **c** on normalized height of application

hand, the nonlinear characteristics of the lateral force distribution were less influenced apart from lowering down the centroid of lateral force distribution. It should be noted that Ito and Matsui's method gave an extremely high resultant lateral force as D_2/D_1 approached to nil, which was also observed by Kumar and Hall (2006) and Ellis et al. (2010). The method of He et al. (2015b) could represent the nonlinear distribution of lateral forces, nevertheless, the magnitude of P_t was still remarkably high, matching closely the values estimated by the Ito and Matsui's method. By comparison, the proposed method could yield a relatively reasonable result that was much smaller than the other two methods at the same pile spacing.

4.5 Effect of depth of unstable soil layer

Figure 15 shows the change in the distribution of lateral forces and the shape of the slip plane against the depth of the unstable soil layer. The normalized depth (h/H) is defined as the ratio of the soil depth to the depth of unstable soil layer. The magnitude of lateral forces increased in proportion to the depth of the sliding soil layer, but the shape of slip plane was less influenced. As the ratio of H/D_1 increased, the nonlinear slip plane gradually turned into a planar having an inclination angle of 52–54°, which ranged between the active slip plane with $\theta = 45° + \varphi/2 \, (=57.5°)$ and the linear one with $\theta = \left[\varphi + \beta + \arccos\left(\sin\varphi / \sin\beta\right)\right]/2 \, (=50.4°)$. Figure 16 demonstrates the variation of the resultant lateral force and the normalized height of application with the depth of the unstable soil layer. More lateral forces were applied onto the piles as H/D_1 increased, and P_t obtained from the other two methods increased more rapidly than the proposed method. The difference in P_t between the other two methods and the proposed method for $H = 2$ m was 271.6 kN, while the value discrepancy significantly increased to be 1235.6 kN for $H = 10$ m. The centroid of lateral force distribution had a slight decrease from $h/H = 0.44$ to 0.39 as H increased from 2 to 10 m.
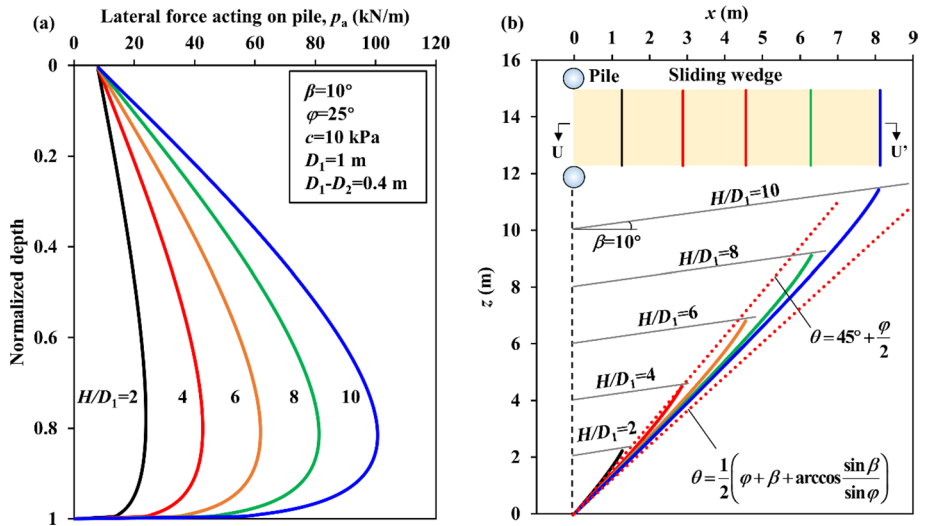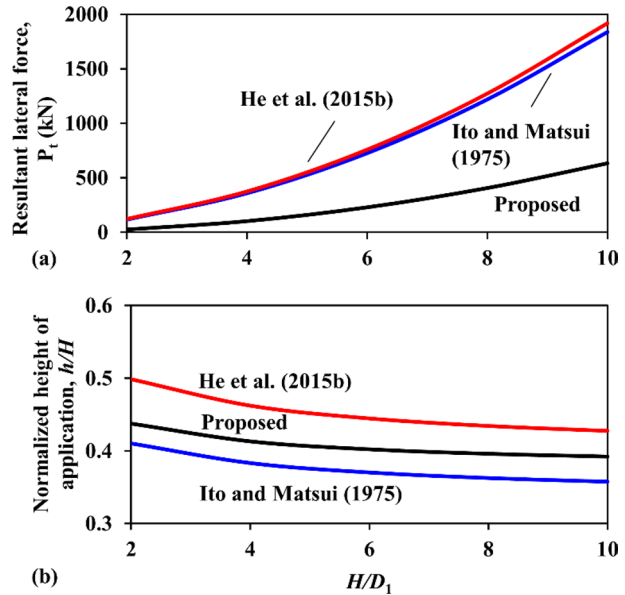
Fig. 15 Effect of the height of the unstable soil layer: **a** on lateral force distribution along the depth; **b** shape of slip plane along the cross section UU′

Fig. 16 Effect of the height of unstable soil layer: **a** on resultant lateral force; **b** on normalized height of application

5 Conclusions

A simplified analytical solution was presented in this paper for estimating the distribution of lateral forces acting on rigid piles embedded in semi-infinite c–φ soil slopes. The soil arching theory was applied to calculate the driving forces transferred onto piles after determining the active lateral earth pressure between neighboring piles through the horizontal

slice method. The applicability of this analytical solution was also evaluated by three experimental case histories and two numerical simulations. Some main conclusions are summarized as follows.

(1) The predicted results from the proposed method were in good agreement with the observed data in terms of both the shape and the magnitude of the distribution of lateral forces. The proposed method was also reliable at small pile spacing compared to the conservative results obtained from the Ito and Matsui's method. As a result, it could be employed in the preliminary prediction of response of piles with scarce design parameters.

(2) The sliding wedge enclosed by the slip plane was deemed to provide the active lateral earth pressure between adjacent piles, serving as an input of force into the arching theory. After analyzing the stress relation of soil elements inside the sliding wedge, it was found that soil cohesion changed the shape of slip plane into a curved one. The nonlinear slip plane in c–φ soil slopes primarily ranged between the active slip plane with $\theta = 45° + \varphi/2$ and the linear one with an inclination angle $\theta = [\varphi + \beta + \arccos(\sin\varphi/\sin\beta)]/2$ to the horizontal.

(3) The distribution of lateral forces along the piles changed from nonlinear to planar as slope angle increased, whereas the remaining parameters (i.e., friction angle, soil cohesion, pile spacing and the height of unstable soil layer) mainly influenced its magnitude. The normalized height of load application developed slightly with these parameters and had an average value of 0.4 which was generally higher than that from Ito and Matsui's method but lower than that from He et al. (2015b)'s method.

Declarations

Conflict of interest The authors have no competing interests to declare that are relevant to the content of this article.

References

Al-Defae AH, Knappett JA (2014) Centrifuge modeling of the seismic performance of pile-reinforced slopes. J Geotech Geoenviron Eng 140(6):04014014. https://doi.org/10.1061/(ASCE)GT.1943-5606.0001105

Ashour M, Ardalan H (2012) Analysis of pile stabilized slopes based on soil-pile interaction. Comput Geotech 39:85–97. https://doi.org/10.1016/j.compgeo.2011.09.001

Cai F, Ugai K (2000) Numerical analysis of the stability of a slope reinforced with piles. Soils Found 40(1):73–84. https://doi.org/10.3208/sandf.40.73

Chen CY, Martin GR (2002) Soil–structure interaction for landslide stabilizing piles. Comput Geotech 29(5):363–386. https://doi.org/10.1016/S0266-352X(01)00035-0

Deng B, Yang M (2019) Bearing capacity analysis of pile-stabilized slopes under steady unsaturated flow conditions. Int J Geomech 19(12):04019129. https://doi.org/10.1061/(ASCE)GM.1943-5622.0001509

Ellis EA, Durrani IK, Reddish DJ (2010) Numerical modelling of discrete pile rows for slope stability and generic guidance for design. Géotechnique 60(3):185–195. https://doi.org/10.1680/geot.7.00090

Guo WD, Ghee EH (2006) Behavior of axially loaded pile groups subjected to lateral soil movement. Found Anal Des 2006:174–181

Hassiotis S, Chameau JL, Gunaratne M (1997) Design method for stabilization of slopes with piles. J Geotech Geoenviron Eng 123(4):314–323. https://doi.org/10.1061/(ASCE)1090-0241(1997)123:4(314)

He Y, Hazarika H, Yasufuku N, Han Z (2015a) Evaluating the effect of slope angle on the distribution of the soil–pile pressure acting on stabilizing piles in sandy slopes. Comput Geotech 69:153–165. https://doi.org/10.1016/j.compgeo.2015.05.006

He Y, Hazarika H, Yasufuku N, Teng J, Jiang Z, Han Z (2015b) Estimation of lateral force acting on piles to stabilize landslides. Nat Hazards 79(3):1981–2003. https://doi.org/10.1007/s11069-015-1942-0

Hewlett WJ, Randolph MF (1988) Analysis of piled embankments. Ground Eng 21(3):12–18

Iskander M, Chen Z, Omidvar M, Guzman I, Elsherif O (2013) Active static and seismic earth pressure for c–φ soils. Soils Found 53(5):639–652. https://doi.org/10.1016/j.sandf.2013.08.003

Ito T, Matsui T (1975) Methods to estimate lateral force acting on stabilizing piles. Soils Found 15(4):43–59

Jeong S, Kim B, Won J, Lee J (2003) Uncoupled analysis of stabilizing piles in weathered slopes. Comput Geotech 30(8):671–682. https://doi.org/10.1016/j.compgeo.2003.07.002

Kahyaoğlu MR, Onal O, Imançlı G, Ozden G, Kayalar A (2012) Soil arching and load transfer mechanism for slope stabilized with piles. J Civ Eng Manag 18(5):701–708. https://doi.org/10.3846/13923730.2012.723353

Kourkoulis R, Gelagoti F, Anastasopoulos I, Gazetas G (2012) Hybrid method for analysis and design of slope stabilizing piles. J Geotech Geoenviron Eng 138(1):1–14. https://doi.org/10.1061/(ASCE)GT.1943-5606.0000546

Kumar S, Hall ML (2006) An approximate method to determine lateral force on piles or piers installed to support a structure through sliding soil mass. Geotech Geol Eng 24(3):551–564. https://doi.org/10.1007/s10706-004-7936-4

Li X, Wei S (2019) A calculation method for the distribution of lateral force acting on stabilizing piles considering soil arching effect. Indian Geotech J 49(1):132–139. https://doi.org/10.1007/s40098-018-0307-5

Li C, Tang H, Hu X, Wang L (2013) Numerical modelling study of the load sharing law of anti-sliding piles based on the soil arching effect for Erliban landslide. China KSCE J Civ Eng 17(6):1251–1262. https://doi.org/10.1007/s12205-013-0074-x

Li F, Hong Z, Yu J, Sun L (2020) Wang L (2020) A novel method of calculating active earth pressure on laggings between piles considering the soil arching effect. Eur J Environ Civ Eng. https://doi.org/10.1080/19648189.2020.1813208

Liang RY, Zeng S (2002) Numerical study of soil arching mechanism in drilled shafts for slope stabilization. Soils Found 42(2):83–92. https://doi.org/10.3208/sandf.42.2_83

Liang RY, Joorabchi AE, Li L (2014) Analysis and design method for slope stabilization using a row of drilled shafts. J Geotech Geoenviron Eng 140(5):04014001. https://doi.org/10.1061/(ASCE)GT.1943-5606.0001278

Lin Z, Dai Z, Su M (2008) Analytical solution of active earth pressure acting on retaining walls under complicated conditions. Chin J Geotech Eng 30(4):555–559 (**in Chinese with English abstract**)

Lin XT, Chen RP, Wu HN, Cheng HZ (2019) Three-dimensional stress-transfer mechanism and soil arching evolution induced by shield tunneling in sandy ground. Tunn Undergr Sp Technol 93:103104. https://doi.org/10.1016/j.tust.2019.103104

Lirer S (2012) Landslide stabilizing piles: experimental evidences and numerical interpretation. Eng Geol 149:70–77. https://doi.org/10.1016/j.enggeo.2012.08.002

Liu X, Cai G, Liu L, Zhou Z (2020) Investigation of internal force of anti-slide pile on landslides considering the actual distribution of soil resistance acting on anti-slide piles. Nat Hazards 102:1369–1392. https://doi.org/10.1007/s11069-020-03971-4

Low BK, Tang SK, Choa V (1994) Arching in piled embankments. J Geotech Eng 120(11):1917–1938. https://doi.org/10.1061/(ASCE)0733-9410(1994)120:11(1917)

Muraro S, Madaschi A, Gajo A (2014) On the reliability of 3D numerical analyses on passive piles used for slope stabilisation in frictional soils. Géotechnique 64(6):486–492. https://doi.org/10.1680/geot.13.T.016

Paik KH, Salgado R (2003) Estimation of active earth pressure against rigid retaining walls considering arching effects. Géotechnique 53(7):643–653. https://doi.org/10.1680/geot.2003.53.7.643

Pirone M, Urciuoli G (2018) Analysis of slope-stabilising piles with the shear strength reduction technique. Comput Geotech 102:238–251. https://doi.org/10.1016/j.compgeo.2018.06.017

Poulos HG (1995) Design of reinforcing piles to increase slope stability. Can Geotech J 32(5):808–818. https://doi.org/10.1139/t95-078

Rui R, Ye YQ, Han J, Zhai YX, Wan Y, Chen C, Zhang L (2022) Two-dimensional soil arching evolution in geosynthetic-reinforced pile-supported embankments over voids. Geotext Geomembr 50(1):82–98. https://doi.org/10.1016/j.geotexmem.2021.09.003

Smethurst JA, Bicocchi N, Powrie W, O'Brien AS (2020) Behavior of discrete piles used to stabilize a tree-covered railway embankment. Géotechnique 70(9):774–790. https://doi.org/10.1680/jgeot.18.P.150

Van Eekelen SJM, Bezuijen A, Van Tol AF (2013) An analytical model for arching in piled embankments. Geotext Geomembr 39:78–102. https://doi.org/10.1016/j.geotexmem.2013.07.005

Viggiani C (1981) Ultimate lateral load on piles used to stabilize landslides. Proc 10th Int Conf Soil Mech Found Eng Sweden 3:555–560

Wang GL (2013) Lessons learned from protective measures associated with the 2010 Zhouqu debris flow disaster in China. Nat Hazards 69:1835–1847. https://doi.org/10.1007/s11069-013-0772-1

Wang C, Wang H, Qin W, Tian H (2021) Experimental and numerical studies on the behavior and retaining mechanism of anchored stabilizing piles in landslides. Bull Eng Geol Environ 80(10):7507–7524. https://doi.org/10.1007/s10064-021-02391-3

Wei S, Sui Y, Yang J (2019) Model tests on anti-sliding mechanism of circular and rectangular cross section anti-sliding piles. Rock Soil Mech 40(3):951–961 (**in Chinese with English abstract**)

Zhao X, Li K, Xiao D (2020) A simplified method to analyze the load on composite retaining structures based on a novel soil arch model. Bull Eng Geol Environ 79(7):3483–3496. https://doi.org/10.1007/s10064-020-01780-4

Zhu MX, Zhang Y, Gong WM, Dai GL (2016) Discussion on Evaluating the effect of slope angle on the distribution of the soil-pile pressure acting on stabilizing piles in sandy slopes. Comput Geotech 100(79):176–181. https://doi.org/10.1016/j.compgeo.2016.04.020